

Demonstrating Improved Multiple Transport-Mean-Free-Path Imaging Capabilities of Light Sheet Microscopy in the Quantification of Fluorescence Dynamics

Matthias Rieckher, Stylianos E. Psycharakis, Daniele Ancora, Evangelos Liapis, Athanasios Zacharopoulos, Jorge Ripoll, Nektarios Tavernarakis, and Giannis Zacharakis*

Optical microscopy constitutes, one of the most fundamental paradigms for the understanding of complex biological mechanisms in the whole-organism and live-tissue context. Novel imaging techniques such as light sheet fluorescence microscopy (LSFM) and optical projection tomography (OPT) combined with phase-retrieval algorithms (PRT) can produce highly resolved 3D images in multiple transport-mean-free-path scales. Our study aims to exemplify the microscopic capabilities of LSFM when imaging protein dynamics in *Caenorhabditis elegans* and the distribution of necrotic cells in cancer cell spheroids. To this end, we apply LSFM to quantify the spatio-temporal localization of the GFP-tagged aging and stress response factor DAF-16/FOXO in transgenic *C. elegans*. Our analysis reveals a linear nuclear localization of DAF-16::GFP across tissues in response to heat stress, using a system that outperforms confocal scanning fluorescent microscopy in imaging speed, 3D resolution and reduced photo-toxicity. Furthermore, we present how PRT can improve the depth-to-resolution-ratio when applied to image the far-red fluorescent dye DRAQ7 which stains dead cells in a T47D cancer cell spheroid recorded with a customized OPT/LSFM system. Our studies demonstrate that LSFM combined with our novel approaches enables higher resolution and more accurate 3D quantification than previously applied technologies, proving its advance as new gold standard for fluorescence microscopy.

1. Introduction

For more than three centuries, optical microscopy has been the basis of all biological studies and discoveries and the method of choice for high resolution imaging of biological tissue. It constitutes one of the most fundamental paradigms in biology and medicine, despite the limitations imposed by the highly diffusive light propagation in tissue, restricting its applicability to superficial investigations in the order of a few millimeter.^[1] Figure 1A shows the effect of light scattering for different regimes in terms of penetration depth, denoted by the transport mean free path (TMFP) and actual distance (mm). The cost of imaging deeper in tissue is very high in terms of resolution, as illustrated vividly in Figure 1B going from cellular, to imaging 3D cell clusters.

Even when modern advances are implemented such as confocal or non-linear methods, the increase in penetration depth is still not enough for adequate deep tissue imaging.^[2,3] Methods that provide three

dimensional microscopic images, such as OPT^[4-6] and LSFM or SPIM^[7-9] have significant advantages compared to traditional methods such as CSFM in imaging larger samples, without though overcoming the main limiting factor of scattering. Even the ground breaking conceptions of super-resolution microscopy or nanoscopy, awarded with the 2014 Nobel Prize, are limited to the depths of conventional microscopy.^[10-12] However, despite the breakthroughs in terms of deep understanding of biological function the effect of multiple scattering has not yet being overcome at least in terms of realistic implementations in deep microscopic imaging.


Most of the efforts in compensating for these effects are directed toward altering the optical properties of tissue with invasive methods such as optical clearing which transform the tissue into a transparent nanoporous hydrogel. The widely used methods of CLARITY^[13] or BABB^[14] produce impressive and high resolution images when combined with modern microscopic techniques.^[15] However, the price to pay for such clarity is severe since the tissue under investigation has been irreversibly damaged.

Dr. M. Rieckher
Institute for Genome Stability in Ageing and Disease, Cologne
Cluster of Excellence in Cellular Stress Responses in Aging-Associated
Diseases (CECAD)
University Hospital Cologne
Cologne 50931, Germany

S. E. Psycharakis, Dr. D. Ancora, Dr. E. Liapis, Dr. A. Zacharopoulos,
Dr. G. Zacharakis
Foundation for Research and Technology Hellas
Institute of Electronic Structure and Laser
N. Plastira 100, Heraklion GR-70013, Crete, Greece
E-mail: zahari@iesl.forth.gr

Prof. J. Ripoll
Department of Bioengineering and Aerospace Engineering
Universidad Carlos III de Madrid
Madrid 28911, Spain

Prof. N. Tavernarakis
Foundation for Research and Technology Hellas
Institute of Molecular Biology and Biotechnology
N. Plastira 100, Heraklion GR-70013, Crete, Greece

 The ORCID identification number(s) for the author(s) of this article can be found under <https://doi.org/10.1002/biot.201700419>.

DOI: 10.1002/biot.201700419

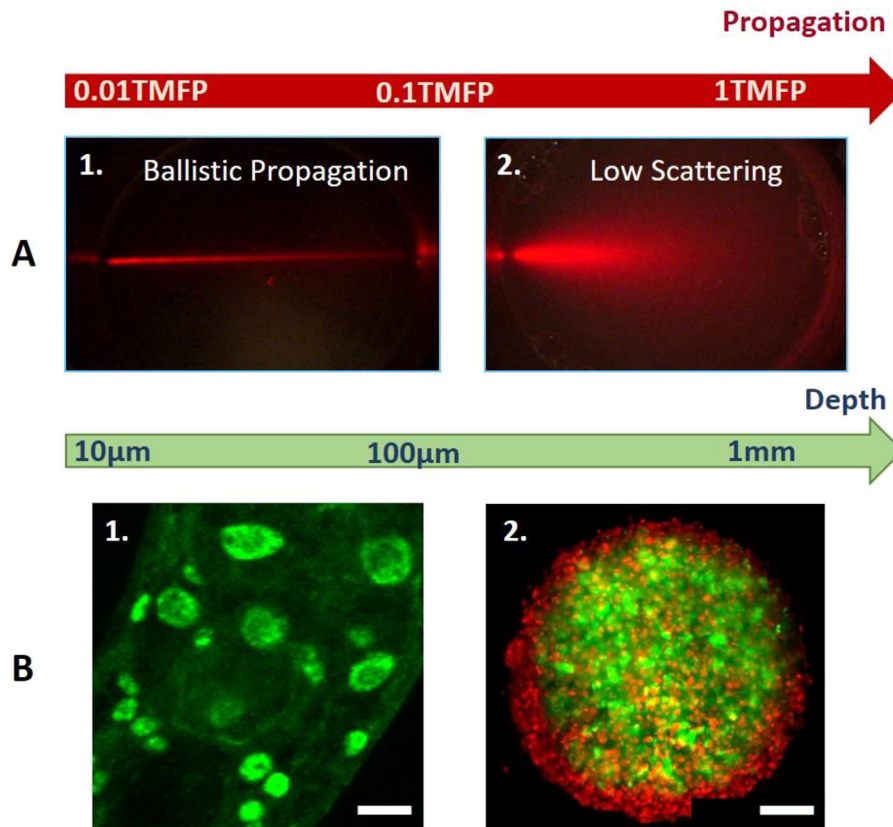


Figure 1. Light propagation through biological tissue across the relevant length scales in terms of scattering and penetration depth. Panel A shows a laser beam propagating through an aqueous solution with increasing scattering properties. Panel B shows characteristic images in the corresponding regimes. (B1) high resolution images of the stress response factor DAF-16::GFP in *C. elegans*. Size bar is 25 μm . (B2) Fluorescence from a doxorubicin-treated GFP-T47D cancer cell spheroid stained with DRAQ7. Size bar is 100 μm .

A radical new approach to overcome the limitations imposed by multiple scattering is to proactively compensate for the refractive index variations in tissue, by applying novel photonic technologies, such as wavefront shaping, in order to manipulate the optical paths producing an equivalent effect to chemical clearing.^[16–19] Furthermore, appropriate algorithms can be implemented for optimization and retrieval of scrambled coherent properties based on physical properties such as intrinsic isoplanatism or memory effect.^[20,21] In fact, the use of novel computational methods has the potential to revolutionize microscopic approaches, enabling the imaging of live samples, and organisms in yet inaccessible regimes of depth and resolution.^[22] These innovative methodologies have yet to be applied in applications involving *in vivo* investigations of living organisms to study various biomedical processes that underlie diseases.

In this manuscript, we demonstrate how LSFM can outperform conventional methods in two scenarios covering multiple transport-mean-free-path regimes. In the first case, LSFM outperforms confocal microscopy when imaging the GFP-tagged DAF-16/FOXO stress response factor in *C. elegans*: LSFM provides quantitative data of fluorescence dynamics with better quality 3D images, increased acquisition speed and reduced photobleaching, resulting in a relatively higher resolved

nuclearization dynamics of DAF-16::GFP upon heat stress. In the second scenario, we demonstrate how the implementation of phase retrieval algorithms in three dimensions can radically improve the performance of LSFM when imaging optically opaque live samples in the form of cancer cell spheroids. We demonstrate how the PRT reconstruction of combined OPT/LSFM data results in uniform resolution throughout the entire volume of the scattering sample. With these two studies, we manage to cover both the microscopic (≈ 1 MFP) and mesoscopic (≈ 1 TMFP) regimes of light transport.

2. Experimental Section

2.1. *C. elegans* Maintenance and 3D Imaging

C. elegans was maintained as previously described.^[23] To visualize DAF-16::GFP nuclearization we used the transgenic strain TJ356 (genotype $zIs[daf-16p::daf-16a/b::GFP;rol-6(su1006)IV]$).^[24] For LSFM, young adult animals were anesthetized with 5 mM levamisole (Sigma–Aldrich, St. Louis, MO, USA) and mounted in 2% low-melting agarose (Sigma–Aldrich) dissolved in PBS buffer that was cooled to room temperature (RT) before use. Animals in solution were transferred into a glass-capillary,

which was fixed to the stage holder of a Lightsheet Z.1 microscope (Carl Zeiss AG, Jena, Germany). To image temperature-dependent nuclear recruitment of DAF-16::GFP the sample chamber was heated from RT to 30 °C, while continuously imaging with a 20x objective (W Plan-Achromat 20x/1.0 DIC, Carl Zeiss AG) every 20 s, producing 37 time points, each with 69 slices (1024 × 1024 pixels) of 1 μm spacing. For CSFM, young adult animals were immobilized in a nanoparticle solution on a 5% agarose pad as previously described^[25] and imaged with a LSM510 laser scanning microscope (Carl Zeiss AG) via a 20x objective (EC Plan-Neofluar 20x/0.50 M27, Zeiss). To produce 3D datasets of a quality comparable to LSFM, we captured 10 time points (scan time 100 s), each with 37 slices (512 × 512 pixels) of 1 μm distance, while heating the environmental chamber from RT to 30 °C. To compare photobleaching of the DAF-16::GFP signal between the systems we imaged transgenic animals at 20 °C continuously for 7.5 min. For LSFM, the GFP signal was excited with a 488 nm laser light sheet at 2.4% laser power, and a laser power of 2.4% at the confocal microscope. We used ZEN 2.3 (blue edition; Carl Zeiss AG) for 3D image generation and ImageJ for analysis.

2.2. Tumor Spheroid Generation and Imaging

Spheroids were generated with the hanging drop method using Perfecta3D 96-well plates (3D Biomatrix, Ann Arbor, MI, USA) following manufacturer's instructions. Four days old spheroids composed of T47D human ductal carcinoma cells (ATCC HTB-133) were incubated at 37 °C for 24 h prior to imaging, with 1.5 μM DRAQ7TM (Biostatus, Leicestershire, UK), a far-red membrane impermeable fluorescent DNA dye that selectively stains the nuclei in dead and permeabilized cells. For imaging, the spheroid was transferred into a FEP tube (800 μm inner diameter, Bola, Germany), which was sealed with self-adhesive putty and loaded on a custom LSFM system and kept into a 37 °C water bath throughout the duration of the experiment.

2.3. Customized OPT/LSFM System

Experiments performed on spheroids were realized with an in-house developed OPT/LSFM system described elsewhere.^[7] The light sheet was shaped by cylindrical optics to a full width at half maximum of 7 μm, with its central plane inside the focal plane of the 10x/0.28 infinity corrected detection objective (Mitutoyo, Japan). Image acquisition was performed through a tube lens and an electron multiplying CCD (Ixon DV885, Andor Technology, Belfast, UK), with a resolution of 1004 × 1002 pixels and pixel size of 8 μm. The pixel size of the imaging system was 0.8 μm. Fluorescence excitation was accomplished by a continuous wave 635 nm diode laser and fluorescence emission was recorded by a 650 nm long pass filter. The sample was imaged at 180 angular positions separated by a step of 2° in order to complete a full rotation and scanned, at each angle, through the light sheet in steps of 20 μm, each composed of 13 slices.

2.4. 3D Autocorrelation

For each LSFM dataset at different angle, we calculated the Average Intensity Projection (AIP) of every frame, then cropped with a squared window of 300 pixels (field of view of 240 μm), constructed the AIP-sinogram, which is aligned by considering the center of mass of each AIP as the center of rotation (as in an OPT experiment) and then backprojected to obtain the reconstruction volume. By calculating its autocorrelation with the Wiener–Khinchin theorem we obtain the autocorrelation sinogram (A-sinogram), which is always aligned.^[22] The A-sinogram can be backprojected with an inverse Radon transformation leading to the reconstruction of a cubic volume which mathematically corresponds to the three-dimensional autocorrelation of the imaged specimen.

2.5. Phase Retrieval Algorithm

PRT is based on the use of Gerchberg–Saxton phase retrieval (PR) algorithms in order to retrieve the phase connected with the autocorrelation, or more appropriately, with the estimation of the modulus of the Fourier transform.^[26] The retrieval of the correct phase through an iterative process passing from the real (or object) space to the Fourier space applying appropriate constraining operations, enables the reconstruction of the whole object. The three-dimensional autocorrelation was used as an estimation of the Fourier modulus of the object to reconstruct, associating a random initial three-dimensional phase as starting point for the iterative Phase Retrieval problem. A mixed Hybrid Input-Output (HIO) approach was used for 5000 steps followed by 1000 steps of Error-Reduction (ER).^[22] The algorithm was implemented in MATLAB with GPU-CUDA extension and typical running time for the reconstruction was about 1 h.

3. Results and Discussion

3.1. Microscopy Regime: LSFM Imaging of Protein Dynamics in *C. elegans*

We demonstrate the capability of LSFM to precisely measure protein dynamics by imaging transgenic *C. elegans* expressing the GFP-tagged transcription factor DAF-16, homolog of human forkhead box O (FOXO) that acts in the insulin/IGF-1-mediated signaling (ILS) pathway. DAF-16 is a master regulator of stress responses that translocates from the cytoplasm to the nucleus, a rapid process that upon heat exposure is standardly visualized in a qualitative manner by light microscopy or CSFM.^[24,27] So far, numerous studies revealed the genetic mechanisms and environmental factors that govern DAF-16 activity and nuclearization, including the evidence for a systemic function across tissues in lifespan-control.^[28] However, little quantitative data are available about its spatio-temporal dynamics in response to heat stress.

We apply a quantitative approach by imaging DAF-16::GFP via LSFM in the anterior part of young adult *C. elegans* that are exposed to increasing heat stress gradually from 20 to 30 °C. Our 3D images show highly resolved DAF-16::GFP nuclearization

across different cell types and tissues (Figure 2A). The image analysis reveals a near-linear recruitment of the transcription factor to intestinal nuclei upon increasing time and temperature (Figure 2B). In parallel, we performed confocal imaging under the same environmental conditions with the goal to obtain similar quality 3D images (Figure 2A). The direct comparison of the datasets produced by the two systems reveals the following major differences: i) LSFM outperforms confocal microscopy in acquisition speed (37 time points vs. 10 time points in approx.

the same time frame), leading to a better resolved measurement of protein dynamics; ii) LSFM produces more image slices in a shorter time (69 slices, 1024×1024 , within 20 s vs. 37 slices, 512×512 , within 100 s) resulting in a higher 3D resolution of the final image. However, CSFM-derived images display a higher resolution and detail in the XY plane. iii) The continuous linear increase of DAF-16::GFP nuclearization observed in LSFM datasets hits a plateau in CSFM datasets after the final temperature of 30°C is reached (Figure 2B). In LSFM, every

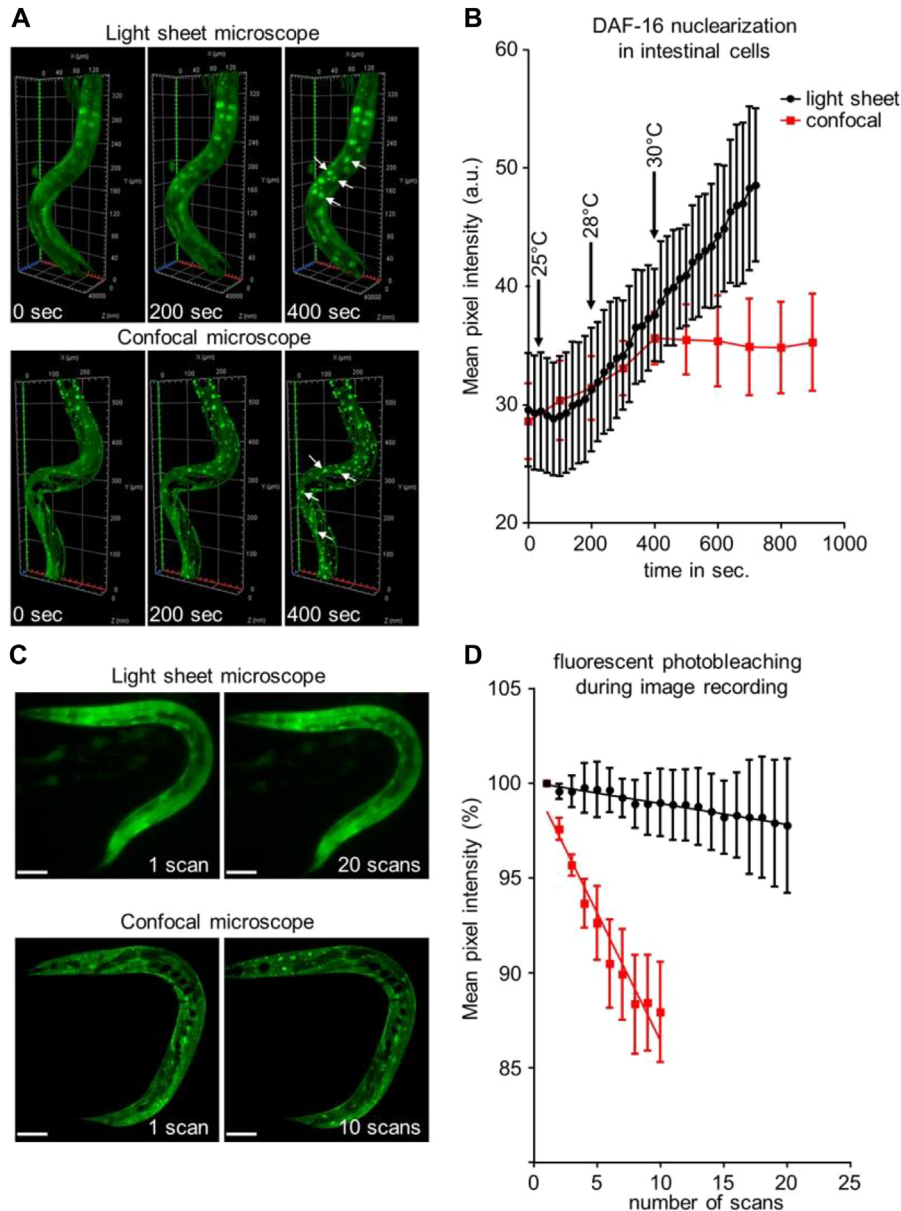


Figure 2. Comparing LSFM with CSFM to measure the dynamics of DAF-16::GFP nuclearization in *C. elegans*. A) Representative 3D images of transgenic *C. elegans* expressing DAF-16::GFP derived from LSFM and CSFM data. The animals were continuously imaged while being exposed to heat stress increasing from RT to 30°C . Arrows indicate intestinal nuclei. B) Quantification of the fluorescent signal in intestinal nuclei ($n=5$) of the individual shown in 2A. C) Representative maximum intensity projections of animals that were imaged for 7.5 min at 20°C with either LSFM (20 time points) or CSFM (10 time points). Size bar is $50\ \mu\text{m}$. D) Quantification of the fluorescent signal of various areas ($n=5$) within the samples in 2C in percent (%) based on the initial fluorescence intensity.

focal plane is illuminated and recorded only once, as opposed to point-by-point scanning in confocal microscopy, which leads to a markedly reduced photo-toxicity within the sample.^[29] Hence, repetitive confocal scanning diminishes the fluorescence signal, masking the continuous DAF-16::GFP nuclearization observed

in LSM. To verify this possibility we quantified the relative fluorescent signal across tissues, in images derived from either modality performed at 20 °C (Figure 2C), revealing a significantly higher reduction of the fluorescence signal in CSFM (Figure 2D).

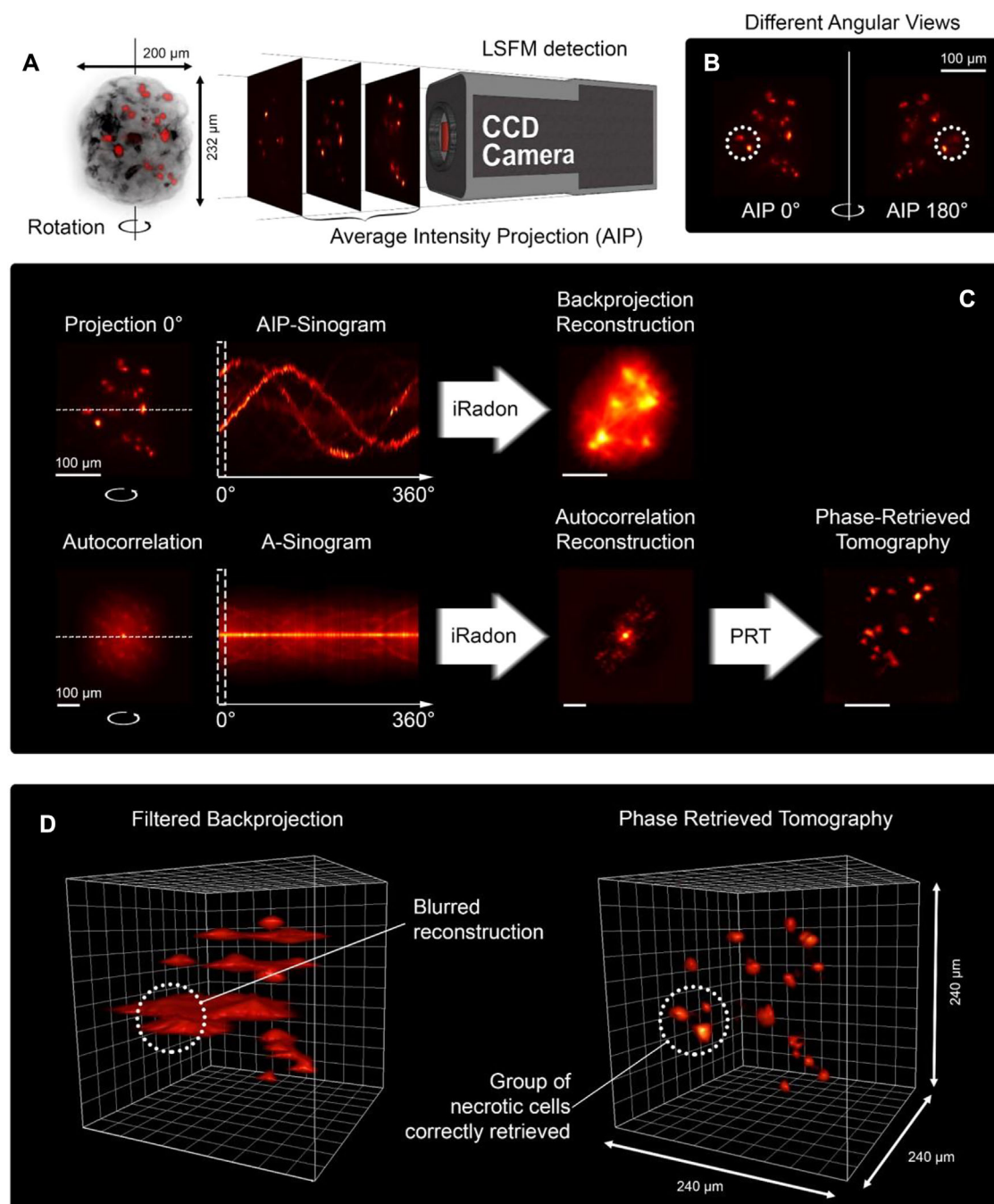


Figure 3. PRT imaging protocol to image fluorescence emission from human tumor spheroid. A) Schematic of the LSFM measurement of a cancer cell spheroid, from which we calculate the AIP at each angle of rotation. B) At opposite angles, fluorescence is hidden due to light diffusion through the specimen. C) Comparison of backprojection reconstructions of the specimen (OPT) and its autocorrelation (PRT). The sinogram shows the rotation of a single line (dashed) in the image. Finally, PRT can reconstruct the object by retrieving the phase associated to such 3D-autocorrelation. The images shown are AIP of the reconstructed volumes looked from the top (tomographic axis). D) Volume-renderings of the direct object reconstruction and from the phase retrieval method.

3.2. Mesoscopy Regime: OPT/LSFM Imaging in Live Cell Spheroids With Phase Retrieval

We have employed the Phase-Retrieved Tomography method to uniquely image the fluorescence distribution of the cell-death marker DRAQ7TM in a tumor spheroid with a diameter of about 200 μm (Figure 3A). Even at these seemingly small sizes, scattering is enough to impose several changes in the photon propagation through the sample. This is clearly visible by the obstruction of superficial fluorescing cells at different angles, as shown in Figure 3B. In terms of scattering this means that light transport is in the regime where thickness >1 TMFP meaning that the measurement is in the mesoscopic regime.

A schematic of the experimental and computational procedures is shown in Figure 3A–C.

The OPT/LSFM system was used to acquire, per each rotation angle, a collection of tomographic slices making sure the whole sample was scanned during each LSFM acquisition. We then compared a traditional OPT reconstruction with our PRT method to demonstrate the ability to retrieve hidden information and achieve uniform resolution. Since the sample is opaque and obstructs the fluorescence distribution differently at each angle, the reconstruction calculated using normal OPT is blurred with very low resolution (top right image of panel 3C). If we use PRT instead, calculating the autocorrelation sinogram, a perfectly aligned three-dimensional autocorrelation of the object is reconstructed, which produces a high resolution reconstruction of the dead cells distribution in the spheroid. Figure 3D, presents the volume rendering for both reconstruction methods, and clearly demonstrates the advantage of PRT compared to traditional OPT, achieving uniform resolution throughout the entire volume of an opaque live tissue sample.^[30–32]

4. Conclusions

In summary, we have studied two microscopic imaging scenarios corresponding to widely different regimes of light propagation and demonstrated how modern LSFM combined with novel computational methods can produce high-quality 3D images with advanced spatio-temporal resolution, accurate quantification, and precise characterization of fluorescence dynamics. On one hand, we have shown that LSFM can outperform conventional CSFM in accurately quantifying and precisely characterizing the translocation of DAF-16::GFP protein upon stress induction, or any fluorescently tagged protein, that dynamically moves within cells and across tissues in *C. elegans*. On the other hand, we have shown how novel 3D PRT methods can extend the imaging abilities of LSFM into the mesoscopic regime, by imaging the distribution of dead cells in an optically opaque cancer cell spheroid, and produce uniform resolution throughout the scattering volume.^[33,34]

Future 3D implementations of LSFM/PRT will extend the depth to resolution ratio to even more inaccessible regimes, drastically improving the current state of the art and shifting the paradigm of modern biomedical imaging.

Abbreviations

3D, three dimensional; *C. elegans*, *Caenorhabditis elegans*; CSFM, confocal scanning fluorescent microscopy; FEP, fluorinated ethylene propylene; LSFM, light sheet fluorescent microscopy; OPT, optical projection tomography; PRT, phase retrieved tomography; RT, room temperature; SPIM, selective plane illumination microscopy; TMFP, transport mean free path.

Acknowledgements

This work was supported by the EU Marie Curie ITN “OILTEBIA” (PITN-GA-2012-317526), the H2020 LASERLAB Europe (EC-GA 654148), and the FP7 Project FMT-XCT (GA 201792). J.R. acknowledges support from the EC FP7 CIG grant HIGH-THROUGHPUT TOMO, and MINECO grant FIS2016-77892-R. We acknowledge F. Geisler, S. Kant and R. Windoffer from the Institute of Molecular and Cellular Anatomy (MOCA), Uniklinik RWTH Aachen, Germany for access to the Lightsheet microscope Z.1 and technical assistance.

Conflict of Interest

The authors declare no commercial or financial conflict of interest.

Keywords

Caenorhabditis elegans, cancer cell spheroids, light sheet fluorescence microscopy, optical projection tomography, phase retrieved tomography

Received: June 10, 2017

Revised: October 23, 2017

Published online:

- [1] V. Ntziachristos, *Nat. Methods* **2010**, *7*, 603.
- [2] D. J. Stephens, V. J. Allan, *Science* **2003**, *300*, 82.
- [3] W. R. Zipfel, R. M. Williams, W. W. Webb, *Nat. Biotechnol.* **2003**, *21*, 1369.
- [4] J. Sharpe, U. Ahlgren, P. Perry, B. Hill, A. Ross, J. Hecksher-Sorensen, R. Baldock, D. Davidson, *Science* **2002**, *296*, 541.
- [5] A. Bassi, B. Schmid, J. Huisken, *Development* **2015**, *142*, 1016.
- [6] A. Arranz, D. Dong, S. Zhu, C. Savakis, J. Tian, J. Ripoll, *Sci. Rep.* **2014**, *4*, 7325.
- [7] M. Rieckher, I. Kyparissidis-Kokkinidis, A. Zacharopoulos, G. Kourmoulakis, N. Tavernarakis, J. Ripoll, G. Zacharakis, *PLoS ONE* **2015**, *10*, e0127869.
- [8] J. Huisken, J. Swoger, F. Del Bene, J. Wittbrodt, E. H. K. Stelzer, *Science* **2004**, *305*, 1007.
- [9] R. M. Power, J. Huisken, *Nat. Methods* **2007**, *14*, 360.
- [10] E. Betzig, G. H. Patterson, R. Sougrat, W. O. Lindwasser, S. Olenych, J. S. Bonifacino, M. W. Davidson, J. Lippincott-Schwartz, H. F. Hess, *Science* **2006**, *313*, 1642.
- [11] S. W. Hell, *Science* **2007**, *316*, 1153.
- [12] F. C. Zanacchi, Z. Lavagnino, M. P. Donnorso, A. Del Blue, L. Furia, M. Faretta, A. Diaspro, *Nat. Methods* **2011**, *8*, 1047.
- [13] K. Chung, J. Wallace, S. Y. Kim, S. Kalyanasundaram, A. S. Andalman, T. J. Davidson, J. J. Mirzabekov, K. A. Zalocusky, J. Mattis, A. K. Denisin, S. Pak, H. Bernstein, C. Ramakrishnan, L. Grosenick, V. Gradinaru, K. Deisseroth, *Nature* **2013**, *497*, 332.

- [14] M. K. Schwarz, A. Scherbarth, R. Sprengel, J. Engelhardt, P. Theer, G. Giese, *PLoS ONE* **2015**, *10*, e0124650.
- [15] M. Docosz, V. Ntziachristos, W. Scheuer, S. Strobel, *Neoplasia* **2014**, *16*, 1.
- [16] A. P. Mosk, A. Lagendijk, G. Lerosey, M. Fink, *Nat. Photonics* **2012**, *6*, 283.
- [17] S. Gigan, *Nat. Photonics* **2017**, *11*, 14.
- [18] D. Di Battista, G. Zacharakis, M. Leonetti, *Sci. Rep.* **2015**, *5*, 17406.
- [19] D. Di Battista, D. Ancora, H. Zhang, K. Lemonaki, E. Marakis, E. Liapis, S. Tzortzakis, G. Zacharakis, *Optica* **2016**, *3*, 1237.
- [20] J. Bertolotti, E. G. van Putten, C. Blum, A. Lagendijk, W. L. Vos, A. P. Mosk, *Nature* **2012**, *491*, 232.
- [21] O. Katz, P. Heidmann, M. Fink, S. Gigan, *Nat. Photon.* **2014**, *8*, 784.
- [22] D. Ancora, D. Di Battista, G. Giasafaki, S. E. Psycharakis, E. Liapis, J. Ripoll, G. Zacharakis, *Sci. Rep.* **2017**, *7*, 11854.
- [23] S. Brenner, *Genetics* **1974**, *77*, 71.
- [24] S. T. Henderson, T. E. Johnson, *Curr. Biol.* **2001**, *11*, 1975.
- [25] E. Kim, L. Sun, C. V. Gabel, C. Fang-Yen, *PLoS ONE* **2013**, *8*, e53419.
- [26] Y. Shechtman, Y. C. Eldar, O. Cohen, H. N. Chapman, J. Miao, M. Segev, *IEEE Signal Process. Mag.* **2015**, *32*, 87.
- [27] K. Lin, H. Hsin, N. Libina, C. Kenyon, *Nat. Genet.* **2001**, *28*, 139.
- [28] N. Libina, J. R. Berman, C. Kenyon, *Cell* **2003**, *115*, 489.
- [29] E. H. Stelzer, *Nat. Methods* **2015**, *12*, 23.
- [30] P. J. Verveer, J. Swoger, F. Pampaloni, K. Greger, M. Marcelllo, E. H. K. Stelzer, *Nat. Methods* **2007**, *4*, 311.
- [31] F. Pampaloni, N. Ansari, E. H. K. Stelzer, *Cell Tissue Res.* **2013**, *352*, 161.
- [32] C. Lorenzo, C. Frongia, R. Jonard, J. Fehrenbach, P. Weiss, A. Maandhui, G. Gay, B. Ducommun, V. Lobjois, *Cell Div.* **2011**, *6*, 22.
- [33] J. Andilla, R. Jonard, O. E. Olarte, A. C. Dufour, M. Cazales, Y. L. E. Montagner, R. Ceolato, N. Riviere, J. C. Olivo-Marin, P. Loza-Alvarez, C. Lorenzo, *Sci. Rep.* **2017**, *7*, 44939.
- [34] D. Ancora, D. Di Battista, G. Giasafaki, S. E. Psycharakis, E. Liapis, J. Ripoll, G. Zacharakis, *Methods* **2017**, in press, <https://doi.org/10.1016/j.ymeth.2017.10.009>